Article:

Meacock, O.J. orcid.org/0000-0001-6269-9855, Doostmohammadi, A., Foster, K.R. et al. (2 more authors) (2021) Bacteria solve the problem of crowding by moving slowly. Nature Physics, 17 (2). pp. 205-210. ISSN 1745-2473

https://doi.org/10.1038/s41567-020-01070-6

Supplementary information for ‘Bacteria solve the problem of crowding by moving slowly’

O. J. Meacock, A. Doostmohammadi, K. R. Foster, J. M. Yeomans, W. M. Durham

Nature Physics (2020)

Contents

Supplementary Notes

Both our experimental observations and mechanistic models show that the increased force generated by hyperpiliated Δ*pilH* cells causes them to become preferentially trapped in rosettes, which impairs their ability to spread (Fig. 4, Extended Data Figs. 5-7, Supplementary Videos 5, 7-9). However, aside from hyperpiliation, the deletion of *pilH* could have other effects on cells that may affect their ability to compete with WT cells within colonies. In the first three sections of the following note, we discuss experiments and analyses that show that differences in growth rate, cell-cell adhesion, and cell length are not sufficient to explain our results. This is followed by a discussion of the potential role of chemotaxis. We then describe experiments in which we supress cell verticalization with progressively stiffer agar to directly test whether rosette formation is responsible for the loss of Δ*pilH* cells from the front of mixed colonies. Finally, we review the multiple lines of evidence that support our conclusions.

1. Growth rate

Individual Δ*pilH* cells move more quickly than individual WT cells (Fig. 1e, Extended Data Fig. 3), likely because they express a larger number of pili on their surface[17,51]. Δ*pilH* cells also exhibit increased levels of 3',5'-cyclic adenosine monophosphate (cAMP)[52], which is a secondary messenger known to increase pilus production, in addition to affecting a large number of other cellular processes[52,53]. Thus, it is plausible that Δ*pilH* cells could grow more slowly than WT cells. To investigate this possibility, we competed YFP labelled Δ*pilH*, Δ*pilB* and WT cells with a CFP labelled WT reference strain in liquid culture. While Δ*pilH* cells are hyperpilated compared to WT cells, Δ*pilB* cells lack pili on their surface[17]. In addition, we used the competition between the two differently labelled WT strains as a negative control. We counted the number of CFUs after 0, 3.5, and 7 h of incubation (Methods), allowing us to resolve the fitness of the YFP labelled test strains relative to the WT reference strain over the same timescale as used in our subsurface colony assays (Extended Data Fig. 8b). Our results show that both Δ*pilH* cells and Δ*pilB* cells have no detectable difference in growth relative to WT cells over these timescales ($p > 0.05$, one-sample t-test, $n = 3$, Methods).

2. Cell-cell adhesion

Our experiments show that motility driven by Type IV pili greatly enhances the expansion rate of *P. aeruginosa* colonies (Fig. 1f, g, Supplementary Video 3). However, Type IV pili have also been shown to increase cell-cell adhesion in colonies of *Neisseria gonorrhoeae*, which are composed of spherical cells that expand primarily by cell division, and in rafts of swarming *P. aeruginosa*, which use flagella to collectively swim in a thin film of liquid[24,25]. In both cases, non-piliated strains are pushed to the outer edge of the colony because they exhibit reduced cell-cell adhesion compared to WT cells.

To test whether increased cell-cell adhesion might impede the outward migration of strains with more pili in our experiments, we inoculated subsurface colonies with equal fractions of piliated WT and non-piliated Δ*pilB* cells. In contrast to previous studies[24,25] we found that the WT cells gradually displaced non-piliated Δ*pilB* cells from the front as the colony expanded (Extended Data Fig. 9a-c). These results suggest that pili predominantly act to enhance the rate of *P. aeruginosa* colony spreading via collective motility, rather than reducing it via increased cell-cell adhesion.

We also tested if intercellular adhesion played role in the accumulation of Δ*pilH* cells within rosettes. Because Δ*pilH* cells are hyperpilated, one might expect them to adhere to one another more strongly than WT cells, preferentially inhibiting their outwards migration. To investigate this possibility, we studied the movement of Δ*pilH* cells at low density so that we could resolve the interaction between individual cells.

Cell movement was tracked three hours after inoculation in a subsurface colony. At this stage, cells were highly motile but the majority were spaced far apart from one another. We then isolated (*i*) events where previously separated cells came into contact with one another and (*ii*) events where cells already in contact moved away from one another. If cells actively adhered to each other, we would expect that cells would both slow down after contacting one another and increase their speed after moving away from one another.

We manually isolated 41 events where a previously isolated cell came into contact with another cell and 47 events where two cells already in contact moved apart (Extended Data Fig. 9d). We then measured the speed of cells as they underwent these two types of events. The set of timeseries was aligned such that the timepoint at which contact was made or broken occurred at $t = 0$, and the speed of cells undergoing each type of event was then averaged across time.

For both categories of cell movement, we observed a peak in cell speed at $t = 0$ because movement is required for either event to be detected (Extended Data Fig. 9d). Importantly however, there was no discernible difference in the speed of cells before or after either event. Moreover, the two time series from cells making contact and breaking contact with one another are indistinguishable, suggesting that cell adhesion is negligible. Visual inspection of individual cells also failed to reveal any evidence of aggregation or changes in motility behaviour during cell-cell contact. These results suggest that cell-cell adhesion does not play a substantial role in the collective movement of Δ*pilH* cells.

This finding is consistent with our observation that Δ*pilH* cells in densely-packed collectives move faster than solitary ones (Extended Data Fig. 3), indicating that the hyperpilation of Δ*pilH* cells enhances collective motility rather than stifling it through enhanced cell-cell adhesion. Moreover, our experiments indicate that the collision of comets drives an inward migration of cells towards points that ultimately form rosettes (Fig. 4d-f, Extended Data Fig. 7, Supplementary Video 9), suggesting that rosette formation involves active motility rather than passive aggregation driven by increased adhesion.

3. Aspect ratio

We observed that Δ*pilH* cells appeared to be somewhat longer than WT cells when in monoculture (e.g. Supplementary Video 6). To verify this, we imaged both genotypes when mixed together in a single monolayer, ensuring that both experienced the same environmental conditions. We used confocal fluorescence microscopy to identify the differently labelled genotypes and measured the size of cells by fitting them with ellipses. This analysis confirmed our initial observation: Δ*pilH* cells had an average length of 3.64 µm (n = 217), whereas WT cells had an average length of 3.12 µm (n = 223). The difference in measured cell length was significant ($p < 10^{-10}$, Mann-Whitney *U* test). Similar findings were observed for (*i*) solitary cells at low density in the subsurface assay and (*ii*) in liquid cultures growing at exponential phase (Extended Data Fig. 6a). Taken together, these analyses show that Δ*pilH* cells are longer than WT cells across a wide range of conditions. While the mechanisms involved are not known, we speculate the enhanced cAMP concentrations found in Δ*pilH* cells[52] may play a role.

The aspect ratio of individual agents has been observed to impact the collective behaviours that arise from both passive cell growth[22,54] and active motility[15] in groups of densely-packed rods. To understand how differences in cell length might impact rosette formation we used our 3D SPR model to simulate monolayers composed of cells with different aspect ratios ($a =$ 3.5, 4, and 5), spanning the range observed in our experiments (Extended Data Fig. 6a). We varied the force, F, exerted by each of these different rods and quantified both the mean rod speed and fraction of vertical rods at steady state (Extended Data Fig. 6b, c). These results show that longer rods have a *decreased* tendency to reorient out of plane for a given F (Extended Data Fig. 6c). Consequently, monolayers composed of longer rods can propel themselves with a larger force, F, before they begin to buckle out of plane, allowing them to achieve a larger mean speed (Extended Data Fig. 6b). Mechanistically, this occurs because rotating a longer cell out of plane requires a larger deformation of the elastic materials that act to stabilize the horizontal orientation of the cells (i.e. the overlaying agar and the polymeric secretions that glue cells to surfaces). We predict that the torque required to rotate a cell into a vertical orientation increases with its length squared (Eq. *S*7c), suggesting that small increases in cell length could dramatically stifle rosette formation.

Our analyses therefore indicate that the increased length of Δ*pilH* cells actually make it harder for them to rotate out of plane and form rosettes. Thus, the increased force generated by Δ*pilH* cell causes them to preferentially form rosettes *in spite* of their longer length. This finding is consistent with previous work on non-motile *Vibrio cholerae* colonies, which also found that longer cells are more resistant to verticalization than shorter ones[22].

To confirm that these findings from monoculture simulations could be extended to mixed genotype situations, we performed additional SPR simulations that model the interaction between cells with different lengths. To approximate WT and Δ*pilH* cells, we considered rods with an aspect ratio of $a_1 = 4$ and $a_2 = 5$, which approximate experimental measurements of the WT and Δ*pilH,* respectively (Extended Data Fig. 6a). In contrast to the simulations presented in Fig. 4b, where we quantified the interactions between rods with the same aspect ratio and different F, the simulations presented in Extended Data Fig. 6d kept the force generated by the "WT cells" constant and varied the force generated by the longer "Δ*pilH* cells" (i.e. "WT cells" have fixed aspect ratio $a_1 = 4$ and self-generated force $F_1 = 1.5$, whereas "Δ*pilH* cells" have fixed $a_2 = 5$ and exert a variable force, F_2). As anticipated from the monoculture simulations, in cases that F_2 exceeded F_1 by a small amount the longer rods were able to move faster than the shorter rods on average. However, once F_2 increased beyond a critical threshold the longer cells were preferentially trapped within rosettes, which reduced their relative mean speed. Compared to our simulations where both populations had the same length ($a_1 = a_2 = 4$, Fig. 4b), we observed that rosette formation was triggered at a larger value of F_2 owing to the increased stability of the longer "Δ*pilH* cells" ($a_1 = 4, a_2 = 5$, Extended Data Fig. 6d). Interestingly, we found that once the critical value of F_2 is exceeded, a larger aspect ratio actually *increases* the representation of "Δ*pilH* cells" in rosettes (Extended Data Fig. 6d, e). In other words, a larger aspect ratio allows cells to exert more force before forming rosettes, but once this critical threshold is crossed the longer cells are more likely to become trapped in the resulting rosettes than the shorter ones. This observation is consistent with our experiments, which show that the higher force and longer Δ*pilH* cells are much more likely to end up in rosettes than the lower force and shorter WT cells (Fig. 4f). The increased representation of longer cells within rosettes is also consistent with longer cells having a stronger tendency to align with their neighbours, which in this case are vertically oriented. Similar effects are widely observed in the context of nematic alignment in liquid crystals, in which a larger aspect ratio leads to a larger orientational elasticity[55,56] and therefore stronger alignment.

In conclusion, we observe that Δ*pilH* cells are longer than WT cells. The greater length of Δ*pilH* cells stabilizes them against rosette formation, so they have to generate an even larger force before they can nucleate rosettes. However, once rosettes form, the longer length of Δ*pilH* cells increases their representation in rosettes relative to the shorter WT cells.

4. Chemotaxis

Chemotaxis allows bacteria to direct their motility towards more favourable chemical environments. One might speculate, therefore, that WT cells migrate outwards faster than Δ*pilH* cells in colonies because the latter cannot effectively perform chemotaxis. While *P. aeruginosa* can perform chemotaxis using either flagella[57] or pili[18], previous work has shown that deleting *pilH* has no effect on flagella-based motility or flagella-based chemotaxis[51]. This, taken together with our experiments with flagellar mutants (Extended Data Fig. 1a, b), indicates that the slower expansion rate of Δ*pilH* colonies does not stem from an inability to perform flagella-based chemotaxis.

PilH is one of two response regulators in the Pil-Chp signal transduction system that regulates pili extension/retraction[18], suggesting that Δ*pilH* cells might lack the ability to perform pili-based chemotaxis. While appreciable chemical gradients could arise in our colonies at late stages, we observe that WT cells overtake *ΔpilH* mutants after only 6 hours (Fig. 2f). At this early stage of development, the colony is composed of a ~3 micron thick monolayer of cells overlaid with a 3,000 µm thick layer of nutrient-rich LB agar, suggesting radial nutrient gradients are negligible compared to those found in the agar-based assays classically used to study flagella-based chemotaxis[58]. Moreover, we observe that the fraction of Δ*pilH* cells at the colony edge first increases at the beginning of the experiment, but then precipitously drops at the moment the monolayer reaches confluence and cells transition from individual to collective movement (Fig. 2d-g). This suggests that rosette formation, rather than a deficiency in single-cell chemotaxis, is responsible for the loss of *ΔpilH* cells at the edge of colonies. Indeed, increased cell density would be expected to disrupt the chemotaxis of WT cells because cell-cell interactions act to reorient individual cells (Supplementary Video 6), which would inhibit their ability to bias the length of their runs[18]. Thus, if the outwards movement of WT cells in our colonies was being guided by chemotaxis, one would expect that the onset of collective motility would act to reduce their advantage over *ΔpilH* cells, rather than to enhance it, as we observe.

Although the above theoretical arguments suggest that chemotaxis is unlikely to play a role in the loss of Δ*pilH* cells from the edge of colonies, we also sought to experimentally investigate whether chemotaxis contributes to the expansion of the colonies in our assays. It has been previously shown that the Δ*pilG* mutant cannot perform chemotaxis at the glass-liquid interface in microfluidic devices[18]. We found that Δ*pilG* cells form subsurface colonies that expand much more slowly than the WT (Extended Data Fig. 1a,b). However, while Δ*pilG* and WT cells move at similar speeds in microfluidic devices[18], in these high friction agar-based assays Δ*pilG* cells display little, if any motility (Extended Data Fig. 1c). This is likely because Δ*pilG* cells express few pili compared to WT cells[17]. More generally, the Pil-Chp system regulates both chemotaxis and pilus production in this species[17,18,52] , making it difficult to separate these two processes.

Although we could not use a genetic mutant to definitively test whether chemotaxis plays a role in colony expansion, in the following section we describe experiments in which we directly test how rosette formation affects the persistence of Δ*pilH* at the front of mixed Δ*pilH*/WT colonies. These results demonstrate that rosette formation, rather than pili-based chemotaxis or another unanticipated mechanism, is responsible for the loss of Δ*pilH* from the front.

5. Supressing rosettes increases the persistence of Δ*pilH* cells at the colony front

In our subsurface experiments, cells are sandwiched between agar and a glass surface; to form rosettes cells must rotate vertically and deform the agar above them. Increasing the concentration of agar dramatically increases its stiffness[49] and thus enhances the agar's ability to keep cells oriented flat against the glass surface[28]. Previous work has shown that increasing the concentration of agar neither alters the diffusion rate of nutrients[59], nor the intrinsic growth rate of bacteria in subsurface colonies[28]. We therefore reasoned that if the preferential trapping of Δ*pilH* cells in rosettes causes them to be depleted from the colony front, increasing the agar concentration would allow Δ*pilH* cells to persist for longer at the front by suppressing vertically oriented rosettes.

We inoculated subsurface colonies with equal fractions of Δ*pilH* and WT cells onto 0.8%, 1.2% and 1.6% agar pads. Nanoindentation measurements suggest that 1.6% agar has a Young's modulus approximately four times greater than that of 0.8% agar[49], which our simple model predicts will lead to a four-fold increase in the stabilising torque that keeps the rod-shaped cells flat against the glass surface (Eq. *S*7c). We then used our automated image-analysis pipeline, colEDGE (Supplementary Fig. 1, Supplementary Methods), to quantify the packing fraction (ρ) and the fraction of Δ*pilH* cells (f_H) within the colony front. Experiments were performed in triplicate, yielding a total of nine colonies across the three different agar concentrations.

Although the bacterial culture used to inoculate all of these cultures was prepared in an identical way (Methods), the distribution of cells at the beginning of our experiments varied between colonies. As the liquid bacterial culture used to inoculate these colonies evaporates, cells are deposited along the outer rim of the drop, a process known as the 'coffee ring' effect[60]. As this process is driven by evaporation, it was difficult to precisely control how many cells ended up collecting along the edge of the dried droplet and we observed that the starting cell density at the outer rim of the colony tended to be larger for increased agar concentrations. To account for this variability, we aligned all our data sets using our measurements of cell packing fraction. Specifically, we fit our packing fraction data with a function of the form:

$$\left.\begin{array}{r}\rho(r_{\mathrm{SUB}}) = Pe^{\mu(r_{\mathrm{SUB}}-r_{\mathrm{C}})} \\ \rho(r_{\mathrm{SUB}}) = P \qquad\qquad\end{array}\right\} \begin{array}{l} r_{\mathrm{SUB}} \le r_{\mathrm{C}} \\ r_{\mathrm{SUB}} > r_{\mathrm{C}}\end{array} \qquad (S1)$$

to determine, r_{C}, the colony radius at which the cells become confluent (i.e. fully packed together) at the front. Here, r_{SUB} is the colony radius, P is the maximal packing fraction (≈ 1) and μ is the characteristic length scale over which ρ increases. We then aligned data from each colony using r_{C}, which collapsed the trace of ρ from all colonies onto a single curve (Extended Data Fig. 10a). This alignment process thus allows us to control for the variations in the initial density of cells at the colony front and directly compare f_{H} across different colonies that are at a similar stage of development (Extended Data Fig. 10b).

While the fraction of Δ*pilH* cells at the front decreased once the colony reached confluence for all three agar concentrations, we observed that Δ*pilH* cells were able to migrate considerably further with larger concentrations of agar. For example, increasing the concentration of agar from 0.8% to 1.6% increased the fraction of Δ*pilH* cells in the front by 80 fold once colonies had expanded 1200 µm from the point at which they reached confluence ($r_{\mathrm{C}} + 1200\,\mu m$, Extended Data Fig. 10b, inset). The 1.2% agar condition showed an intermediate response, with 10-fold more Δ*pilH* cells than the 0.8% agar colonies at the same location. In general, colonies grown under stiffer agar retained significantly more Δ*pilH* cells (at $r_{\mathrm{C}} + 1200\ \mu\mathrm{m}$, *n* = 9, *p* < 0.005, Spearman's rank correlation test). While our image analysis provides rigorous quantification, the different proportions of Δ*pilH* cells within the front under these different conditions can also readily be observed by eye in the raw images (Extended Data Fig. 10c).

To test whether the suppression of rosettes was responsible for the increased persistence of Δ*pilH* cells, we imaged the distribution of Δ*pilH* cells immediately behind the front as the colony reached confluence (Extended Data Fig. 10d, e). As in our previous experiments, we observed that under 0.8% agar Δ*pilH* cells aggregated into discrete, spot-like rosettes and that these rosettes increased in size over time. Groups of Δ*pilH* cells also initially formed under 1.6% agar, but these were unstable and were later "smeared" by the collective movement of neighbouring cells. This smearing creates elongated plumes of horizontally oriented Δ*pilH* cells, from which they could subsequently resume collective movement. This indicates that while 1.6% agar acts to prevent rosettes from fully trapping Δ*pilH* cells in place, the movement of Δ*pilH* cells is still impeded relative to that of WT cells.

More broadly, these experiments directly show that supressing rosette formation increases the ability of Δ*pilH* cells to persist at the front of an expanding colony, which supports our hypothesis that rosettes play a critical role in how different bacterial strains compete with one another on surfaces.

Concluding remarks

Our supplementary analyses show that differences in growth rate, cell-cell adhesion, and cell aspect ratio cannot explain why Δ*pilH* cells are overtaken by WT cells when mixed together in colonies. Conversely, we find that:

(i) Individual Δ*pilH* cells move faster than WT cells in the subsurface environment (Fig. 1e, Extended Data Fig. 3).

(ii) When colonies are inoculated with equal fractions of WT and Δ*pilH* cells, the fraction of Δ*pilH* cells in the front initially increases when cells move individually, but begins to decline at the same time at which the front becomes confluent and rosettes begin to form (Fig. 2d-g, Supplementary Video 5).

(iii) We directly observe that Δ*pilH* cells are preferentially trapped in rosettes in both subsurface (Fig. 4f) and surficial colonies (Extended Data Fig. 2c).

(iv) Our mechanistic models demonstrate that when faster and slower cells are mixed together under densely-packed conditions, the faster moving cells preferentially become trapped in vertically oriented rosettes (Fig. 4b, Extended Data Fig. 6d). The rosettes in these simulations bear close resemblance to the rosettes observed in our experiments (Fig. 4c, Extended Data Fig. 6e).

(v) Experiments with stiffer agar are observed to both supress rosette formation and significantly increase the persistence of Δ*pilH* cells in the colony front (Extended Data Fig. 10).

Thus, multiple lines of evidence indicate that the increased force generated by Δ*pilH* cells causes them to become preferentially trapped in rosettes, which limits their ability to collectively spread.

Supplementary Methods

1. Protocols for subsurface assays

The evaporated droplet of cell culture used to initialize colonies contains a dense band of cells along its outer edge due to the "coffee ring" effect[60], while the interior of the evaporated droplet contains cells at much lower density. Analyses that investigated cells at low densities (Extended Data Figs. 1c, 3b, 6a, 9d) were based on cells in this interior region. Over time, cell division increases the density of cells within the interior and the colony front begins to expand outward. In our assays that quantify the dynamics of these expanding colonies (Figs. 1f, g, 2c-g, Extended Data Figs. 1a, b, 9a-c, 10, Supplementary Videos 3, 4), we used the dense outer band of cells on the edge of the evaporated droplet as the reference point from which to measure the colony radius, r_{SUB}. Assays that measure the movement of cells in the monolayer of colonies (Figs. 1e, 3, Extended Data Figs. 3a, 4, Supplementary Videos 2, 6) were performed in colonies that had reached the steady-state expansion regime (Fig. 1g).

To monitor the expansion of colonies containing only a single strain (Fig. 1f, g, Extended Data Fig. 1a, b, Supplementary Video 3), we inoculated four colonies at different positions on a single agar pad and used the motorized stage on the Zeiss inverted microscope to move between them at each imaging timepoint, allowing us to collect data from multiple genotypes simultaneously. In all cases, one of the four colonies was a WT control. Each colony was imaged using a tile of eight adjacent fields of view, the first of which was centred on the band of aggregated cells at the edge of the "coffee ring" described above. Eight brightfield images were acquired for each colony every two minutes over a period of 11 h. These experiments used a relatively low magnification (20X) to minimize the number of fields of view needed, allowing us to acquire data for multiple colonies simultaneously.

For subsurface colonies containing two different fluorescently labelled strains (Fig. 2c-g, Extended Data Figs. 9a-c, 10), we inoculated 1 µL of the mixed culture onto an agar pad. Because these liquid-grown, exponential phase cells had relatively weak YFP and CFP signals, colonies were incubated at room temperature for 2.5 h prior to imaging to allow fluorophores to accumulate. Colonies were imaged with the Zeiss inverted microscope. The colony edge was imaged using a tile of 20 adjacent fields of view, the first of which was centred on the edge of the colony at the start of imaging. To obtain a spatial resolution sufficient to estimate both cell packing fraction and genotypic composition, we used a 63X objective. The colony was imaged at ten-minute intervals to avoid phototoxicity and bleaching over the course of the 8 h long experiment.

To track the movement of individual cells in the monolayer of colonies (Figs. 1e, 3, Extended Data Figs. 3a, 4, Supplementary Videos 2, 6), we spotted monocultures of WT and Δ*pilH* cells onto separate agar pads. These were incubated overnight at room temperature (16 h) to allow the colony expansion to reach the steady-state regime (Fig. 1g). We then acquired 150X magnification (100X objective, with 1.5X zoom) brightfield images of the monolayer using the

Nikon inverted microscope at a framerate of one image per second, yielding sufficient temporal and spatial resolution for single-cell tracking.

We also quantified the movement and size of individual cells at small packing fractions (Extended Data Figs. 1c, 3b, 6a, 9d) using separate subsurface experiments. In the centre of the inoculation spots, cell packing fractions were approximately 50-fold smaller than observed in the monolayer of a subsurface colony at steady-state, so cell-cell interactions were negligible[15]. To ensure cells had sufficient time to adapt to the surface[61], we began imaging 3 h after inoculation. For these low-density experiments, we used the 63X objective and a framerate of one second on the Zeiss inverted microscope.

2. Quantifying the spatiotemporal development of subsurface colonies using the colEDGE image analysis package

2.1 Measuring subsurface colony expansion rates

We developed an image analysis pipeline to quantify the dynamics of colonies as they spread across the surface (Supplementary Fig. 1). Initially, we used Fiji to normalize the local contrast of each brightfield image (Supplementary Fig. 1a). We then used our custom colEDGE Matlab scripts to carry out all subsequent operations.

In the first stage of the colEDGE pipeline, texture analysis is used to separate the regions of the image containing the bacterial colony from the background regions without cells (Supplementary Fig. 1d). Specifically, we measure the standard deviation of pixel intensities within a square neighbourhood centred on each pixel. Portions of the image that include cells contain a wider range of intensities than regions without cells, resulting in a larger standard deviation. Next, to account for variations in the global intensity of the brightfield channel over time and space, we normalise the standard deviation by dividing it by the square root of the mean pixel intensity calculated within the same square window. The resulting texture metric is then thresholded to obtain a binary image that delineates the regions of the image containing cells from cell-free regions.

Ridge detection[40] is next applied to the brightfield images to segment tightly-packed cells, which allows us to accurately distinguish one cell from another (Supplementary Fig. 1e). The ridge image is then binarized using a second threshold, inverted, and combined with the binary texture segmentation described above using a pixelwise "AND" operation to generate the final cell segmentation (Supplementary Fig. 1h). Segmented images from adjacent fields of view are then stitched together to create a single contiguous image at each timepoint.

Because the edge of the colony can undulate (see finger-like protrusions in Supplementary Video 3), we divide the segmented image into twenty strips across its width and locate the position of the colony edge in each by measuring where the cell density rapidly increases. We define r_{SUB} as the median of these twenty measurements. The colony expansion rate, $\frac{dr_{\mathrm{SUB}}}{dt}$, is calculated by taking the gradient of r_{SUB} and applying a smoothing filter to reduce high frequency noise.

2.2 Defining the "front" and "homeland"

In the experiments where we competed fluorescently labelled WT and Δ*pilH* cells in subsurface colonies (Fig. 2c-g, Extended Data Fig. 10), we quantified the genotypic composition and cell packing fraction in both the "homeland" and the "front".

The homeland is defined as the region between r_{SUB} = -10 µm and -60 µm at $t = 0$ (Fig. 2c, Supplementary Video 4), (i.e., inside the evaporated drop of bacterial culture that was used to inoculate the colony). The position of the homeland remains fixed over the course of the experiment.

The front moves as the colony expands and is defined as the region that extends from the leading edge of the colony to 50 µm behind the leading edge. To account for undulations in the leading edge of the colony, we again subdivide the width of the image into twenty strips, which can translate independently from one another (Supplementary Video 4). This allows us to more accurately measure the properties of cells at the periphery of the colony and avoid including the virgin agar beyond the leading edge of the colony in our automated analyses.

2.3 Areal packing fraction measurements

To quantify how tightly packed cells are in the homeland and front regions, we calculate the areal packing fraction, which is defined as the proportion of the two-dimensional surface covered by cells. We note that the same number of rod-shaped *P. aeruginosa* cells can generate different areal packing fractions depending on both their orientations relative to the surface and if they are piled on top of one another. For example, after the monolayer of a colony becomes confluent (i.e. densely-packed), the areal packing fraction may plateau even as the total number of cells per unit area continues to increase as the rod-shaped cells are realigned perpendicular to the surface.

We calculate cell packing fraction using the binary cell segmentation images (Supplementary Fig. 1h). While the dark lines between densely-packed cells allow us to distinguish individual cells, they inaccurately suggest that small gaps exist between touching cells. To generate a more accurate representation of the fraction of the image that is covered by cells, we fill these gaps using morphological closure. The resulting binary image (Supplementary Fig. 1g) is then used to calculate how the packing fraction in the front and homeland of the colony changes over time.

2.4 Measuring changes in the genotypic composition of colonies

To quantify how the relative abundances of different strains in the homeland and front of mixed colonies changes over time (Fig. 2f, Extended Data Figs. 9c, 10b), we developed an automated pipeline to identify YFP and CFP labelled cells. We first perform flatfield correction on both the YFP images (Supplementary Fig. 1b) and CFP images (Supplementary Fig. 1c), before stitching them together to form a continuous image at each time point of the entire imaged region in both channels (YFP, I_Y, and CFP, I_C).

In our subsurface colony experiments (except those in which we varied the agar concentration, see below), the front of subsurface colonies is predominantly composed of a monolayer of cells only one layer thick, allowing each pixel in the stitched images to be assigned as being within a CFP-expressing cell, a YFP-expressing cell, or part of the background without cells. To automatically assign a pixel to one of these three categories, we begin by calculating the YFP/CFP ratio, I_Y/I_C, for each pixel in the image (Supplementary Fig. 1f). The brightfield segmentation (Supplementary Fig. 1h) is then used to determine which of these pixels correspond to cells and which correspond to the background. The distribution of I_Y/I_C for the "within-cell" pixels contains two well-defined peaks (Supplementary Fig. 1f, inset), corresponding to YFP labelled cells and CFP labelled cells. We fit the I_Y/I_C distribution with a two population Gaussian mixture model, allowing us to automate the process of finding the threshold that best discriminates between the two genotypes (Supplementary Fig. 1i). To calculate the fraction of Δ*pilH* cells within the front and homeland regions, we calculate the number of pixels occupied by YFP labelled cells within each region and divide it by the total number of "within-cell" pixels.

We developed a separate genotypic composition quantification method for those experiments in which we varied the agar concentration (Extended Data Fig. 10), as the front of colonies more readily forms multiple layers at higher agar concentrations (Extended Data Fig. 10c). This allows both YFP and CFP labelled cells to occupy the same pixel, breaking our previous assumption that each “within-cell” pixel corresponds to only one of the two genotypes. To calculate how the fraction of the two genotypes changes in the front over time, we exploit the fact that fluorescence intensity tends to increase linearly with the thickness of the colony, which allows us to estimate of the number of layers of YFP and CFP-expressing cells found at each pixel within the colony front. The thin band of cells between r_{SUB} = 0 µm and r_{SUB} = -0.8 µm (one cell width from the colony edge) is consistently a single cell in thickness, regardless of the agar concentration of the overlying pad. Similar to our approach for monolayer data, we calculate a histogram of the ratio of YFP to CFP intensities within this one cell thick region and fit it with a Gaussian mixture model to automatically assign pixels as belonging to either a YFP or CFP-expressing cell. We then calculate s_Y, the average YFP intensity within a single layer of YFP labelled cells, and s_C, the average CFP intensity within a single layer of CFP labelled cells. To account for "crosstalk", which causes YFP labelled cells to appear slightly brighter than regions without cells in CFP images (and vice-versa), we also calculate c_Y, the average intensity of a single layer of YFP labelled cells in the CFP channel, and c_C, the average intensity of a single layer of CFP labelled cells in the YFP channel. We also account for the non-zero background of the fluorescent images by calculating b_Y, the mean pixel intensity in regions of the YFP image where no cells are present and, b_C, the mean pixel intensity in regions of the CFP image where no cells are present. We calculate each of these variables at each time point, allowing us to correct for temporal variations in fluorescence intensity (e.g. those caused by photobleaching).

We now calculate N_Y and N_C, respectively the number of layers of YFP and CFP-expressing cells found within each pixel of the colony front, as:

$$N_Y = \left[\frac{I_Y - b_Y - (c_C\,(I_C - b_C)/s_C)}{s_Y}\right], \qquad (S2a)$$

$$N_C = \left[\frac{I_C - b_C - (c_Y\,(I_Y - b_Y)/s_Y)}{s_C}\right], \qquad (S2b)$$

where the square brackets, $[\cdot]$, indicate a function that rounds to the nearest integer. The last term in the numerator of these equations, $(c_{C,Y}\,(I_{C,Y}\;-\;b_{C,Y})/s_{C,Y})$, corrects for signals from cells with the opposite fluorescent label. Although the cross-talk fluorescence intensity $c_{Y,C}$ is typically small relative to $s_{Y,C}$, this correction is helpful when accounting for native siderophore secretions (produced by all cells) that tend to appear in CFP channel. Both N_Y and N_C are integrated over the entire area of the front to estimate the total volume of YFP labelled cells and total volume of CFP labelled cells, respectively. Lastly, we calculate f_{H} as the volume of YFP cells divided by the volume of CFP cells (Extended Data Fig. 10b).

3. Quantifying topological defects using the Defector software package

The Defector package is a set of Matlab scripts that allow measurement of the positions, orientations and topological charges of +1/2 and -1/2 defects, given the local orientation of the image θ_i at each pixel location i. As described in the main methods section, these values can be measured using the tensor method[44].

Defect locations in the orientation field are detected using a discretized version of the standard path integral definition of a topological defect[10]. The topological charge, n, of each pixel is calculated as

$$n = \frac{1}{2\pi}\sum_{i=2}^{9}[\theta_i - \theta_{i-1}], \qquad (S3)$$

where θ_i is the cell orientation field at each of the 8 neighbouring pixels, where $\theta_9 = \theta_1$ so that the neighbouring pixels form a continuous path. By definition, we order $\theta_1, \theta_2, \dots \theta_9$ so they are ordered sequentially in an anticlockwise direction. This calculation is repeated for each pixel in the orientation field, except for those grid points along the edge of the field of view that are missing neighbours. Defect cores are detected as positions with non-zero values of n, with n = +½ at the location of comets, n = -½ at the location of trefoils, and n = 0 everywhere else.

Having located the defects and determined their charges, we next determine their orientations. To do this, we first define a set of positions $\boldsymbol{r}$ that form an approximately circular path 5 pixels from the defect core. We then calculate the angle $\varphi(\boldsymbol{r})$ from the defect core to each of these positions and compare it to the value of the orientation field $\theta(\boldsymbol{r})$ at that position. The defect orientation is defined to be the value of $\varphi(\boldsymbol{r})$ at which the difference between $\varphi(\boldsymbol{r})$ and $\theta(\boldsymbol{r})$ is smallest[62].

4. Self-propelled rod (SPR) simulations

4.1 Motivation for individual-based modelling approach

Nematic systems have been modelled with a variety of different individual-based and continuum techniques[50,63,64]. When choosing which modelling framework to use to investigate our experimental system, we considered the following factors:

- First, we needed a modelling framework that could capture cells in both the fully two-dimensional configuration that occurs at the beginning of our experiments, and during rosette formation where cells rotate out of the plane.
- Second, the cells in our experiments propel themselves using pili, which attach to a surface and retract to pull the body along[7]. This form of motility is intrinsically different to swimming motility, where cells propel themselves by exerting a force upon the fluid that is then balanced by hydrodynamic drag[65]. Hydrodynamic screening imposed by the nearby no-slip surface will render our experimental system "dry"[15,64,66], i.e. the hydrodynamic flow fields generated by cells are negligible and neighbouring cells align with each other via purely steric interactions.
- Third, rod-shaped *P. aeruginosa* cells are rigid. Unlike some bacterial species, whose bodies are flexible (e.g. *Myxococcus xanthus*[67]), *P. aeruginosa* cells maintain their straight morphologies even when packed together (Supplementary Video 6).
- Fourth, we observed that isolated Δ*pilH* and WT cells move at different speeds (Extended Data Fig. 3) and have slightly different aspect ratios (Supplementary Notes, Extended Data Fig. 6a). We therefore required a model that allows cells with these differing properties to be mixed together in a single simulation.

With these considerations in mind, we decided that an individual based, Self-Propelled Rod (SPR) model[15,47] would allow us to best capture the processes occurring in our experiments. Our simulations model each cell as a rigid chain of Yukawa segments, with segments of different rods repelling one another with a Coulomb-like point potential. This repulsive interaction prevents rods from overlapping, simulating the steric interactions that occur between neighbouring cells. Varying the number of Yukawa segments in each rod allows us to simulate cells with different aspect ratios, while varying the propulsive force exerted by each rod allows us to simulate cells that move at different speeds.

We initially implemented a version of the SPR model in which the orientation of rods was confined to a two-dimensional plane. This allowed us to simulate monolayers of cells prior to rosette development and facilitated direct comparison with a two-dimensional continuum model of active nematics (see section 5, 'Continuum-based modelling' below). To simulate rosette formation, we subsequently extended our SPR model to allow rods to rotate out of the plane (see section 4.3, 'Three-dimensional SPR model' below).

4.2 Two-dimensional SPR model

Model Formulation

Following the governing equations presented in[47], we model cells as rigid rods composed of a fixed number of equally spaced Yukawa segments. Each rod is denoted by the index α. A rod's centroid is given by $\boldsymbol{r}_\alpha = (x_\alpha, y_\alpha)$ and its orientation is given by the unit vector, $\hat{\boldsymbol{u}}_\alpha$, which, when rods are confined to two dimensions, can be described by a single angle, θ_α. We define l_α as the length of α, n_α as the number of Yukawa segments in α, and λ as the screening length, the characteristic length scale over which the repulsive interaction between two segments decays. The characteristic aspect ratio of rod α is then given by $a_\alpha = l_\alpha/\lambda$.

The interaction potential, $U_{\alpha\beta}$, between two rods (denoted by subscripts α and β respectively) is the sum of the interaction between each of their respective Yukawa segments:

$$U_{\alpha\beta} = \frac{U_0}{n_\alpha n_\beta} \sum_{i=1}^{n_\alpha} \sum_{j=1}^{n_\beta} \frac{e^{-r_{\alpha\beta}^{ij}/\lambda}}{r_{\alpha\beta}^{ij}}, \qquad (S4)$$

where $r_{\alpha\beta}^{ij} = \left(\left(x_\alpha^i - x_\beta^j\right)^2 + \left(y_\alpha^i - y_\beta^j\right)^2\right)^{\frac{1}{2}}$, is the Euclidian distance between the segments i and j in rods α and β respectively, and U_0 is the potential amplitude. The total interaction potential for each rod, U_α, is then equal to the sum of all of the interactions between α and all of the other rods in the simulation.

The equations of motion that describe the translation and rotation of each rod are respectively:

$$\boldsymbol{f}_T \cdot \frac{\partial \boldsymbol{r}_\alpha}{\partial t} = -\frac{\partial U_\alpha}{\partial \boldsymbol{r}_\alpha} + F\hat{\boldsymbol{u}}_\alpha, \qquad (S5a)$$

$$f_\theta \frac{\partial \theta_\alpha}{\partial t} = -\frac{\partial U_\alpha}{\partial \theta_\alpha}, \qquad (S5b)$$

where $\boldsymbol{f}_T$ is the translational friction tensor, f_θ is the rotational friction constant and F is the size of the force exerted by a rod along its axis. We use the formulation presented in[47] to calculate $\boldsymbol{f}_T$ and f_θ, which are in turn a function of the rod aspect ratio, a_α, and the Stokesian friction coefficient, f_0.

Implementation of simulations

Our SPR model was implemented in Matlab. Following the approach of[15] we set λ = 1, F = 1 and f_0 = 1. The dynamics of this SPR model have previously been shown to only weakly depend upon the potential amplitude U_0, provided its value is sufficiently large to prevent rod-rod crossing. We used U_0 = 250, which falls within this range[15]. Our simulations were initialized with all rods in uniformly spaced rows and with their orientations aligned with the *y*-axis. Each rod was randomly assigned a movement direction (i.e. half of the rods exerted a force along +*y* and half along –*y*). After an initial transient, this arrangement of rods quickly gives rise to a system that exhibits local nematic ordering that is directed in random directions. We ensured that all simulations reached a statistical steady-state before using their output in our analyses.

We calculated the packing fraction of rods, ρ, in our simulations as the total area of all rods divided by area of the computational domain. In keeping with previous studies[15,47], we modelled the rods as stadia (i.e. as rectangles with semi-circular caps on either end) of length l_α and width λ. This yields:

$$\rho = \frac{1}{A}\sum_{\alpha=1}^{N}\left[\lambda(l_\alpha - \lambda) + \frac{\pi\lambda^2}{4}\right], \qquad (S6)$$

where N is the number of rods ($10^3 < N < 10^4$) and A is the total area of the computational domain. Our simulations correspond to $\rho = 0.25$, which for $F = 1$ produced collective behavior similar to that which was observed in the WT monolayer. We note that the characteristic length scale of repulsion of the Yukawa segments, λ, is an approximation of rod "width", so a domain containing a very tightly packed assemblage of rods could potentially yield $\rho > 1$.

We integrated the governing equations using the midpoint method and periodic boundary conditions. The timestep used ($\Delta t = 0.2$) provided numerically stable results for all sets of simulation parameters tested. To ensure that our results were independent of the size of our domain, we fixed the system density at $\rho = 0.25$ and varied the number of rods, N. We found the rod speed and verticalization were independent of the number of rods in our simulation provided that $N > 10^3$.

Simulating the flow around topological defects using the 2D SPR model

We used our two-dimensional SPR model to predict the movement of cells around comets and trefoils (Fig. 3d). We set $N = 5000$ and chose an aspect ratio $a = 4$ to match the morphology of WT cells in high-density monolayers (Extended Data Fig. 6a). To ensure that the experiments and simulations were analysed in the same way, we used the simulations to generate an image of rod positions at each timepoint and then used OrientationJ to detect topological defects. However, we obtained rod trajectories directly from the simulation output, rather than via cell tracking software. To compare our experiments with simulations, we normalized the dimensions of the former by cell width and the latter by λ, similar to previous studies[15].

4.3 Three-dimensional SPR model

Simulation of rosette formation required that the SPR model be extended into the third dimension to allow rods to reorient vertically. To achieve this, we introduce a new variable, the angle ϕ_α relative to the *xy*-plane. As our confocal imaging suggests that cells reorient out the plane without forming multiple layers during rosette formation (Fig. 4f), in our simulations we ensure that simulated rods remain within a monolayer by prescribing that $z_\alpha = 0$ for all t, where z_α is the *z*-coordinate of rod α.

To define the equation of motion for ϕ_α, we begin by calculating the torque about the centroid of rod α that acts to rotate it out of the *xy*-plane. This torque is generated by steric interactions with surrounding rods and is proportional to the potential gradient $-\frac{\partial U_\alpha}{\partial \phi_\alpha}$. Note that this is analogous to the term $-\frac{\partial U_\alpha}{\partial \theta_\alpha}$ in Eq. ($S5b$), which similarly drives the rotation of rods in the *xy*-plane.

To rotate out of plane, cells must overcome the stabilizing effect of the adhesive secretions that act to glue cells to the surfaces (i.e., extracellular polymeric secretions[48]). In the subsurface assay the overlaying agar also acts to keep the long axis of cells flat against the glass surface[28]. To simulate the resistance to rotation exerted by both cell secretions and agar, we incorporate a physically-based stabilizing torque into our three-dimensional model that acts to keep rods flat against the surface.

Both polymeric secretions and agar have been shown to generate a linearly elastic restoring force when they are deformed on length scales equivalent to that of bacterial cells[49,68]. To simulate the influence of this elastic response on the dynamics of ϕ_α, we assume that the substrate generates a force proportional to the upwards displacement of the tilting rod. This will generate a restoring force equal to $kl_\alpha \sin\phi_\alpha$ at the rod's tip, where k is the elastic modulus of the substrate. Transforming this into a torque acting on the centroid of rod α and adding the torque imposed by the surrounding rods, we arrive at the final equations of motion for the rod, α:

$$\boldsymbol{f}_T \cdot \frac{\partial \boldsymbol{r}_\alpha}{\partial t} = -\frac{\partial U_\alpha}{\partial \boldsymbol{r}_\alpha} + F\hat{\boldsymbol{u}}_\alpha, \tag{$S7a$}$$

$$f_\theta \frac{\partial \theta_\alpha}{\partial t} = -\frac{\partial U_\alpha}{\partial \theta_\alpha}, \tag{$S7b$}$$

$$f_\phi \frac{\partial \phi_\alpha}{\partial t} = -\frac{\partial U_\alpha}{\partial \phi_\alpha} + \frac{kl_\alpha^2}{2}\cos\phi_\alpha \sin\phi_\alpha\,. \tag{$S7c$}$$

The friction constant f_ϕ provides viscous damping for reorientations out of the plane; we assume that viscosity is equal in all directions, i.e. that $f_\phi = f_\theta$. This new model therefore contains one new parameter, k, the elastic modulus of the substrate that resists verticalisation. In practice, we set $k = 0.6$, ensuring the transition to 3D rosette formation occurs over the range of self-propulsion forces $1 < F < 2$. Similar behaviours are observed for other values of k, except the transition occurs at other values of F.

3D SPR model of comet collision

To conceptualize how the collision of +½ defects (comets) gives rise to rosettes, we initialized three-dimensional SPR simulations with two comets directed towards one another (Fig. 4a, Supplementary Video 7). Simulations were initialized as a 12 by 12 lattice of evenly spaced rods, but in contrast to the other simulations described in this section (where rods were randomly initialized along either the +*y* or -*y* direction), rod orientations, θ_α, were initialized using a pre-defined director field such that the two comets pointed towards one other (Fig. 4a). Initial values of ϕ_α were drawn from a normal distribution with zero mean and a standard deviation of 0.5°, which allowed the rods to escape the unstable stationary point at ϕ_α = 0 (Eq. *S7c*). Simulations with different self-propulsion forces, *F*, were run using identical starting configurations. All rods within a given simulation had the same value of *F.*

3D SPR simulations initialized with random rod orientations

To investigate how changes in both cell aspect ratio, *a*, and force generation, *F*, affect rosette formation in more representative disordered monolayers, we performed separate simulations for different values of *F* and *a* (Extended Data Figs. 5, 6b, c, Supplementary Video 8). All rods in a given simulation possessed identical parameters. *N* = 1600 rods were initialized on a 2D lattice in the *xy*-plane, with a small perturbation to ϕ_α as noted in the previous section. This system was allowed to evolve for 300 time steps with $\frac{\partial \phi_\alpha}{\partial t} = 0$, which confined the rods' orientation to the *xy*-plane as they reached a random 2D nematic configuration. We then allowed rods to tilt out of plane and simulated the resulting 3D dynamics for another 2000 time steps. Both the mean rod speed and mean proportion of rods oriented vertically were then calculated over the final 500 time steps of the simulations. While a rod in a perfectly vertical orientation corresponds to ϕ_α = 90°, in practice the orientation of rods within rosettes fluctuate around this value, so we considered a rod to be "vertically oriented" if ϕ_α > 85°. Three simulations were performed for each set of parameter values, each with a different random initial configuration of rods.

3D SPR simulations to explore the interactions between different genotypes

To simulate the interaction between two different genotypes that each generate a different propulsive force, we performed simulations using a similar methodology to that described in the previous section. However, half of the rods propelled themselves with $F_1 = F_v = 1.5$ and the other half with variable F_2 (Fig. 4b, c). To explore how changes in cell length affect the interaction between WT and Δ*pilH* cells, we also performed simulations where we mixed rods that differ in both their force generation and aspect ratio. Half the rods had $a_1 = 4$ and $F_1 = F_v = 1.5$, while the other half had $a_2 = 5$ and exerted a force F_2 that was varied in different simulations (Extended Data Fig. 6d, e).

5. Continuum-based modelling

In addition to our SPR model, we also compared our experimental results with an analytical prediction of the flow of cells around topological defects using a continuum description of active nematics[10,11,69–71]. We used governing equations to describe the coarse-grained velocity $\boldsymbol{u} = (u_r, u_\theta)$ and director fields $\boldsymbol{n} = (n_r, n_\theta)$, the latter representing the orientations of bacteria relative to the center of a defect with charge, m. We considered both trefoils (m = –1/2) and comets (m = +1/2), with each defect occurring at the centre of a circular domain with radius R and a no-slip boundary. This confinement models a defect's interaction with neighbouring topological defects, which act to screen the flow field about it. Despite the polarity of the self-propelled bacteria, the use of a nematic director to describe their orientation is motivated by the emergence of half-integer, nematic, topological defects in the experiments and in the SPR model, which clearly indicate the existence of nematic symmetry within the monolayer. The emergence of such a nematic (apolar) symmetry of a system consisting of polar self-propelled rods is a well-known phenomenon in active matter[72–74].

To analytically calculate the flow field we make several simplifying assumptions, following the approach used in[10]. We assume that:

(*i*) the size of the defect core, a, is much smaller than the screening length scale, R, and that we can therefore neglect variations in the magnitude of the orientational order, (i.e., how strongly the cells are aligned at each point). In reality, the orientational order is zero at the defect core and continuously increases to a finite value, which depends on the thermodynamic properties of the system. Assuming that orientational order around a defect has a uniform magnitude, we can write the director field as:

$$\boldsymbol{n} = (n_r, n_\theta) = (\cos[(m-1)\theta], \sin[(m-1)\theta]), \qquad (S8)$$

where m is –1/2 or +1/2.

(*ii*) We further assume that at steady state the flow field does not alter the director configuration around a defect, so that a separate equation for the evolution of $\boldsymbol{n}$ is not required.

(*iii*) Finally, we assume that the active stresses generated by bacteria dominate over passive elastic stresses that arise due to the orientational deformations around the defect. With this assumption, we can write the Stokes equation simply as a balance of the active force generation and the viscous dissipation:

$$0 = -\boldsymbol{\nabla} p + \eta \boldsymbol{\nabla}^2 \boldsymbol{u} - \zeta \boldsymbol{\nabla} \cdot \left(\boldsymbol{n}\boldsymbol{n}^T - \frac{I}{2} \right), \qquad (S9)$$

where p is the pressure, η is the viscosity, and ζ is the activity coefficient. The direction of flows around defects in our experiments (Fig. 3d) imply that the activity, ζ, is positive, i.e. that our system is extensile. The last term on the right hand side represents the active forces generated by the bacteria and is obtained by coarse-graining the equal and opposite forces arising from self-propulsion and the resistance exerted by the substrate[69,74,75]. Using the form of the director around topological defects from Eq. ($S8$), Eq. ($S9$) can be solved in terms of Green's functions, to yield the velocity field around positive half-integer defects (comets):

$$u_r^{comet} = \left(\frac{\zeta R}{12\eta} - \frac{\zeta}{6\eta} r + \frac{\zeta}{12\eta R} r^2\right) \cos[\theta]\,, \qquad (S10a)$$

$$u_\theta^{comet} = \left(-\frac{\zeta R}{12\eta} + \frac{\zeta}{4\eta} r - \frac{\zeta}{4\eta R} r^2\right) \sin[\theta]\,, \qquad (S10b)$$

whilst for negative half-integer defects (trefoils) we have:

$$u_r^{trefoil} = \left(-\frac{\zeta}{10\eta} r + \frac{3\zeta}{20\eta R} r^2 - \frac{\zeta}{20\eta R^3} r^4\right) \cos[3\theta]\,, \qquad (S11a)$$

$$u_\theta^{trefoil} = \left(\frac{\zeta}{15\eta} r - \frac{3\zeta}{20\eta R} r^2 + \frac{\zeta}{12\eta R^3} r^4\right) \sin\,[3\theta]\,. \qquad (S11b)$$

The details of the algebra are the same as[10] and therefore are omitted here.

Supplementary Video Captions

Supplementary Video 1 | *P. aeruginosa* displays collective motility in surficial colonies. A surficial colony was inoculated with equal proportions of YFP and CFP labelled WT cells. Shown here is the monolayer after 48 h of incubation at room temperature. The left image shows both strains imaged using brightfield microscopy. The right panel shows only the YFP labelled cells. Patterns of collective movement are clearly visible in the right-hand image because only half of the cells are visible. Total duration is 20 mins.

Supplementary Video 2 | Our custom tracking software (FAST) can follow the movement of individual cells even when very tightly packed together. Cyan dots show cell centroids and orange traces show cell trajectories. Total duration is 2 min.

Supplementary Video 3 | Subsurface *ΔpilH* colonies initially expand more quickly than WT colonies, but are eventually overtaken. Brightfield images were background subtracted, inverted and contrast enhanced (Methods). Four adjacent fields of view were recorded and stitched together to form a single image. The dark vertical lines are caused by subtle variations in focus between adjacent fields of view. A colony of Δ*pilB* cells, which lack pili-based motility, is shown as a control. Total duration is 15 h.

Supplementary Video 4 | Quantification of bacterial competition in subsurface colonies using automated image analysis. WT and Δ*pilH* cells were mixed together in equal fractions and used to inoculate a subsurface colony. Automated routines were then used to resolve the location of both the "front" (green boxes) and "homeland" (purple boxes), which were then used in subsequent analyses (Fig. 2d-f). While these datasets also include fluorescent images (Fig. 2g), shown here is the brightfield channel, which is processed as described in the Methods section. Total duration is 8 h.

Supplementary Video 5 | Rosettes in mixed WT and Δ*pilH* colonies are primarily composed of Δ*pilH* cells. The left panel shows the monolayer of a subsurface colony inoculated with an equal proportion of CFP labelled WT cells (grey) and YFP labelled *ΔpilH* cells (yellow). The right panel shows an analogous experiment, but with the opposite labelling *i.e*. with Δ*pilH* cells in grey and WT cells in yellow. The first half of this video shows an overlay of bright field and YFP channels (showing both cell types), while the latter half shows only the YFP labelled cells. Δ*pilH* cells in both experiments become preferentially trapped in rosettes, which appear as yellow patches and dark patches in the left and right panels respectively. To minimize phototoxicity, we did not image the CFP channel in these experiments. Total duration is 3 h.

Supplementary Video 6 | Automated detection of topological defects in WT and Δ*pilH* monolayers. Red circles indicate locations of comet defects (+1/2 charge) and blue triangles trefoil defects (-1/2 charge). Orange arrows and cyan lines indicate the orientation of comets and trefoils, respectively. Total duration is 5 min.

Supplementary Video 7 | The collision of comets generates stable rosettes only if the force exerted by self-propelled rods exceeds a critical threshold. We initialized our 3D SPR model with two comets (red circles, orange arrows) directed towards one another. The initial static image shows the initial configuration of rods. The trefoils (blue triangles) ensure the total topological charge of the system is zero. Rods that propel themselves with a relatively small force ($F = 1$, left) remain horizontally oriented after an initial transient, whereas rods that propel themselves with a larger force ($F = 3$, right) form stable rosettes. Snapshots from these simulations are presented in Fig. 4a.

Supplementary Video 8 | Increased propulsive force causes rosettes to form in a monolayer of rods initialized in a random configuration. Three separate 3D SPR simulations are shown. Rods propel themselves with $F = 0.5$, $F = 1.5$, and $F = 3$ in the left, middle, and right simulations respectively. All other parameters were kept constant between simulations. Data from these simulations are shown in Extended Data Fig. 5a, b.

Supplementary Video 9 | The collision of comets triggers rosette formation in a monolayer composed of both WT and Δ*pilH* cells. This video shows the formation of two different rosettes, in turn. The initial static image in each sequence shows the position of comets (red circles, orange arrows) and trefoils (blue triangles, cyan spokes) prior to rosette formation. In both cases, rosettes are initiated by the collision of two comets. The flowfield generated during the formation of both rosettes is shown in Extended Data Fig. 7a. The first half of the video shows the formation of the rosette presented in Fig. 4d-f; subsequent confocal imaging revealed this rosette was nearly wholly composed of vertically oriented Δ*pilH* cells. Duration of each sequence is 60 min.

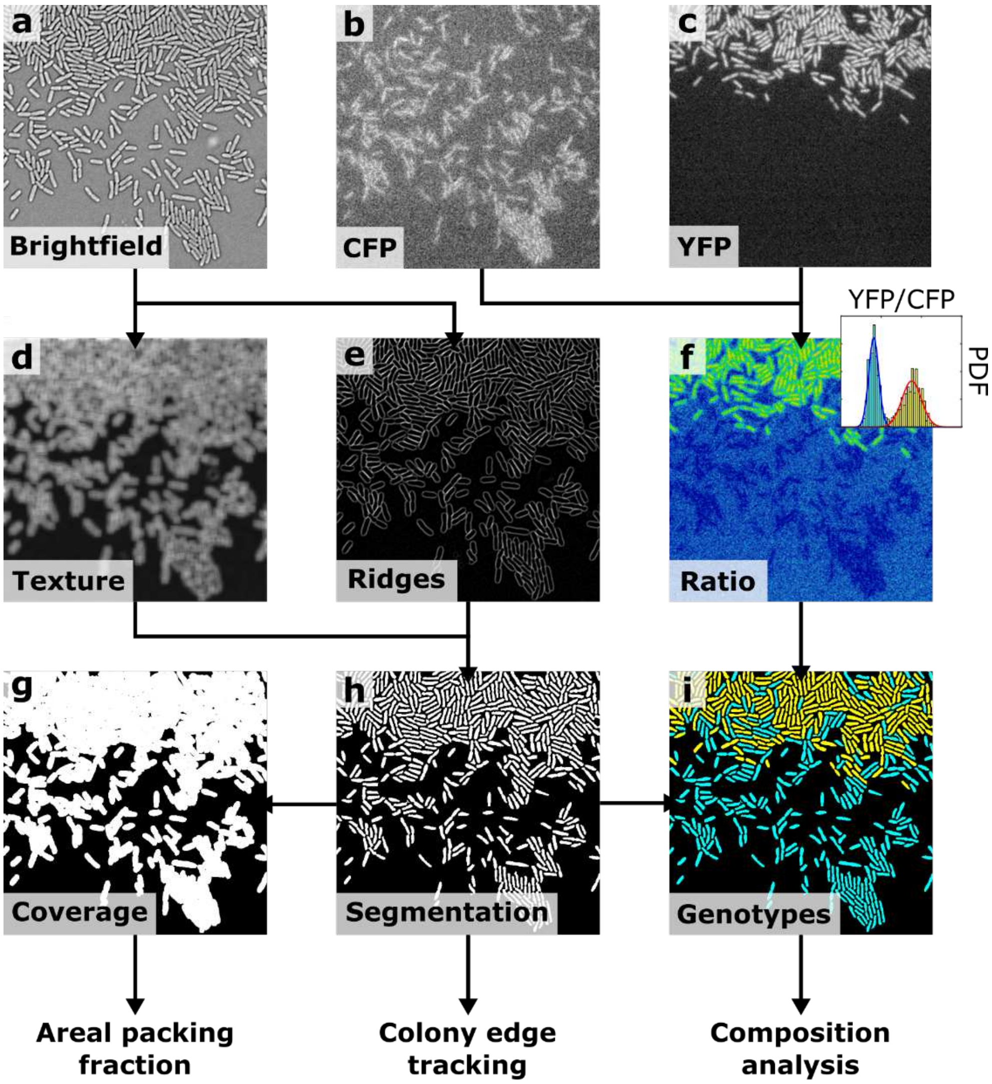

Supplementary Fig. 1 | Automated analysis of subsurface colonies using our custom package colEDGE. a-**c**, We recorded three different images of subsurface colonies at each timepoint: a brightfield image (**a**), a YFP image (**b**) and a CFP image (**c**). **d**, To separate cells from the background, texture analysis (based on a local standard deviation filter, Supplementary Methods) is performed on the brightfield image. **e**, Ridges separating cells are detected in the same image. **h**, These two measures are then thresholded and combined to form a black and white segmentation image, which is used to locate the edge of the colony at each timepoint. **g**, Morphological closure is then applied to this segmented image to generate a cell coverage image, which is used to calculate the areal packing fraction at different positions within the colony. **f**, In a parallel stream, the ratio of YFP to CFP intensity is calculated at each pixel location. The segmentation image (**h**) is then used to remove pixels that are not within cells, allowing us to calculate the distribution of YFP to CFP intensity ratios from only pixels that correspond to cells (inset). This distribution contains two peaks, each corresponding a different genotype. **i**, A Gaussian mixture model is then fitted to this distribution to determine the threshold that best delineates these peaks. Each pixel in the colony segmentation is then assigned to one of the two genotypes on the basis of this threshold, allowing the proportion of each cell type to be measured within different parts of the colony. See Supplementary Methods for additional details.

Microscope name	Model	Camera	Objectives	Lightsources	Additional specifications
'Zeiss inverted'	Zeiss Axio Observer	Zeiss MRm	20X Plan Apochromat air objective 63X Plan Apochromat oil-immersion objective 50X EC Epiplan Neofluar air objective	Zeiss HXP 120 (epifluorescence) Zeiss LSM 700 laser scanning attachment (confocal) Built-in halogen brightfield light source	Definite focus system Zeiss Zen software (Black, confocal, Blue, epifluorescence)
'Nikon inverted'	Nikon Ti-E	Hamamatsu Flash 4.0 v2	100X Plan Apochromat oil-immersion objective	CoolLED pE-100 brightfield light source	Perfect focus system NIS-Elements software
'Zeiss zoom'	Zeiss Axio Zoom. V16	Zeiss MRm	0.5X PlanApo Z air objective 2.3X PlanNeoFluar Z air objective	Zeiss HXP 200 C illuminator (epifluorescence) Built-in brightfield light source	Zeiss Zen software (Blue)

Supplementary Table 1 | Technical specifications of microscopes.

Supplementary References

51. Barken, K. B. *et al.* Roles of type IV pili, flagellum-mediated motility and extracellular DNA in the formation of mature multicellular structures in Pseudomonas aeruginosa biofilms. *Environ. Microbiol.* **10**, 2331–43 (2008).

52. Fulcher, N. B., Holliday, P. M., Klem, E., Cann, M. J. & Wolfgang, M. C. The Pseudomonas aeruginosa Chp chemosensory system regulates intracellular cAMP levels by modulating adenylate cyclase activity. *Mol. Microbiol.* **76**, 889–904 (2010).

53. Persat, A., Inclan, Y. F., Engel, J. N., Stone, H. A. & Gitai, Z. Type IV pili mechanochemically regulate virulence factors in Pseudomonas aeruginosa. *PNAS* **112**, 7563–8 (2015).

54. Smith, W. P. J. *et al.* Cell morphology drives spatial patterning in microbial communities. *PNAS* **114**, E280–E286 (2017).

55. Straley, J. P. Frank Elastic Constants of the Hard-Rod Liquid Crystal. *Phys. Rev. A* **8**, 2181–2183 (1973).

56. Priest, R. G. Theory of the Frank Elastic Constants of Nematic Liquid Crystals. *Phys. Rev. A* **7**, 720–729 (1973).

57. Cai, Q., Li, Z., Ouyang, Q., Luo, C. & Gordon, V. D. Singly flagellated Pseudomonas aeruginosa chemotaxes efficiently by unbiased motor regulation. *MBio* **7**, e00013-16 (2016).

58. Berg, H. C. *E. coli in Motion*. *E. coli in Motion* (Springer New York, 2004).

59. Carnet Ripoche, A., Chollet, E., Peyrol, E. & Sebti, I. Evaluation of nisin diffusion in a polysaccharide gel: Influence of agarose and fatty content. *Innov. Food Sci. Emerg. Technol.* **7**, 107–111 (2006).

60. Deegan, R. D. *et al.* Capillary flow as the cause of ring stains from dried liquid drops. *Nature* **389**, 827–829 (1997).

61. Luo, Y. *et al.* A hierarchical cascade of second messengers regulates Pseudomonas aeruginosa surface behaviors. *MBio* **6**, e02456-14 (2015).

62. Huterer, D. & Vachaspati, T. Distribution of singularities in the cosmic microwave background polarization. *Phys. Rev. D* **72**, 043004 (2005).

63. DeCamp, S. J., Redner, G. S., Baskaran, A., Hagan, M. F. & Dogic, Z. Orientational order of motile defects in active nematics. *Nat. Mater.* **14**, 1110–1115 (2015).

64. Doostmohammadi, A., Adamer, M. F., Thampi, S. P. & Yeomans, J. M. Stabilization of active matter by flow-vortex lattices and defect ordering. *Nat. Commun.* **7**, 10557 (2015).

65. Baskaran, A. & Marchetti, M. C. Statistical mechanics and hydrodynamics of bacterial suspensions. *PNAS* **106**, 15567–72 (2009).

66. Drescher, K., Dunkel, J., Cisneros, L. H., Ganguly, S. & Goldstein, R. E. Fluid dynamics and noise in bacterial cell-cell and cell-surface scattering. *PNAS* **108**, 10940–5 (2011).

67. Harvey, C. W. *et al.* Study of elastic collisions of Myxococcus xanthus in swarms. *Phys. Biol.* **8**, 026016 (2011).

68. Klapper, I., Rupp, C. J., Cargo, R., Purvedorj, B. & Stoodley, P. Viscoelastic fluid description of bacterial biofilm material properties. *Biotechnol. Bioeng.* **80**, 289–296 (2002).

69. Aditi Simha, R. & Ramaswamy, S. Hydrodynamic Fluctuations and Instabilities in Ordered Suspensions of Self-Propelled Particles. *PRL* **89**, 058101 (2002).

70. Marenduzzo, D., Orlandini, E. & Yeomans, J. M. Hydrodynamics and Rheology of Active Liquid Crystals: A Numerical Investigation. *PRL* **98**, 118102 (2007).

71. Marenduzzo, D., Orlandini, E., Cates, M. E. & Yeomans, J. M. Steady-state hydrodynamic instabilities of active liquid crystals: Hybrid lattice Boltzmann simulations. *Phys. Rev. E* **76**, 031921 (2007).

72. Kraikivski, P., Lipowsky, R. & Kierfeld, J. Enhanced Ordering of Interacting Filaments by Molecular Motors. *PRL* **96**, 258103 (2006).

73. Baskaran, A. & Cristina Marchetti, M. Nonequilibrium statistical mechanics of self-propelled hard rods. *J. Stat. Mech. Theory Exp.* **2010**, P04019 (2010).

74. Marchetti, M. C. *et al.* Hydrodynamics of soft active matter. *Rev. Mod. Phys.* **85**, 1143–1189 (2013).

75. Thampi, S. P., Golestanian, R. & Yeomans, J. M. Velocity Correlations in an Active Nematic. *PRL* **111**, 118101 (2013).